Tropical cyclone genesis efficiency: mid-level versus bottom vortex

Xuyang Ge and Tim Li

Department of Meteorology and International Pacific Research Center,

University of Hawaii, Honolulu, HI

Melinda S. Peng

Naval Research Lab., Monterey, CA

Submitted to *Journal of the Tropical Meteorology*

Submitted on August 30, 2011
Revised on Dec. 16, 2011

Corresponding author: Dr. Tim Li, Department of Meteorology, University of Hawaii,

2525 Correa Rd., Honolulu, HI 96822. Email: timli@hawaii.edu

Abstract

Cloud resolving Weather Research and Forecasting (WRF) model simulations are used to investigate tropical cyclone (TC) genesis efficiency in an environment with a near bottom vortex (EBV) and an environment with a mid-level vortex (EMV). Sensitivity experiments show that the genesis timing depends greatly on initial vorticity vertical profiles. The larger initial column integrated absolute vorticity, the greater the genesis efficiency is. For given the same column integrated absolute vorticity, a bottom vortex has higher genesis efficiency than a mid-level vortex.

A common feature among these experiments is the formation of a mid-level vorticity maximum prior to TC genesis irrespective where the initial vorticity maximum locates. Both the EMV and EBV scenarios share the following development characteristics: 1) a transition from non-organized cumulus-scale (~5 km) convective cells into an organized meso-vortex-scale (~50-100 km) system through upscale cascade processes, 2) the establishment of a nearly saturated air column prior to a rapid drop of the central minimum pressure, and 3) a multiple convective-stratiform phase transition.

A genesis efficiency index (GEI) is formulated that include the following factors, initial column integrated absolute vorticity, vorticity at top of the boundary layer and vertically integrated relative humidity. The calculated GEI reflects well the simulated genesis efficiency, and thus may be used to estimate how fast a tropical disturbance develops into a TC.

Key words: Tropical cyclone genesis, mid-level vortex, near bottom vortex, genesis efficiency, cyclogenesis time.

1. Introduction

Tropical cyclone (TC) genesis is the least understood phase in a TC life cycle. Observational studies showed two distinctive genesis precursor scenarios in the western North Pacific (WNP) (e.g., Fu et al. 2007). One is cyclogenesis in an environment with a near bottom vortex (EBV) and the other is cyclogenesis in an environment with a mid-level vortex (EMV). An analysis of the WNP TC genesis in 2000-2001 shows that about 70% (30%) of cyclogenesis events belong to the EBV (EMV) scenario (Fu et al. 2007). Three low-level precursor types have been identified in the WNP. They are: TC energy dispersion induced Rossby wave trains (Holland 1995; Li et al. 2003; Li and Fu 2006; Ge et al. 2010), easterly waves (Chang et al. 1970; Tam and Li 2006; Wang et al. 2010), and northwest-southeast oriented synoptic-scale wave trains (Lau and Lau 1990; Chang et al. 1996).

In contrast to the EBV scenario where the atmospheric precursor signals appear near the surface, TC genesis events associated with the EMV occur when the precursor disturbances appear initially in the middle or upper troposphere. Considerable studies have been devoted to the genesis associated with mid-level precursors in past decades (e.g., Bosart and Sanders 1981; Zhang and Fritsh 1987; Chen and Frank 1993; Ritchie and Holland 1997; Simpson et al. 1997; Bister and Emanuel 1997; Rogers and Fritsch 2001; Houze et al. 2009). Figure 1 illustrates a mid-level precursor genesis example. Typhoon Usagi formed in the South China Sea on 9 August 2001. Three days prior to the genesis, a large amount of cloud liquid water as measured from the Tropical Rainfall Measurement Mission (TRMM)

Microwave Image (TMI) had already appeared over the cyclogenesis region. However, from the QuikSCAT-derived surface wind observations, there was no significant precursor cyclonic wind perturbation (top-right panel). An examination of the National Center for Environmental Prediction (NCEP) global final analysis product reveals a closed cyclonic flow in the mid-troposphere (middle-right panel). This is consistent with the vertical profile of relative vorticity in the region, which shows a vorticity maximum at 650 hPa. Associated with this mid-level vortex is a cold (warm)-core structure below (above) the level (bottom-right panel).

There are two major hypotheses regarding how an initial mid-level vortex generates sufficient surface cyclonic vorticity and forms a sustainable cyclone. A top-down hypothesis assumes direct downward vorticity development (e.g., Bister and Emanuel 1997), whereas a bottom-up hypothesis (e.g., Hendricks et al. 2004; Reasor et al. 2005; Montgomery et al. 2006; Houze et al. 2009) emphasized the role of deep convective "vortical hot towers" (VHTs) in generating lower tropospheric cyclonic vorticity. The difference between the two hypotheses lies essentially on what are the relative roles of stratiform and convective rainfall components in the cyclogenesis process.

An interesting question regarding the EBV and EMV scenarios is which precursor vortex is more efficient in TC genesis. In this study, by designing a number of numerical experiments using a cloud-resolving model with different initial vortex vertical profiles, we intend to address the cyclogenesis efficiency issue. The overall objective of the present study is to investigate the development characteristics and key

differences between mid-level and low-level precursors and to investigate what initial vorticity and humidity conditions favor a more efficient cyclogenesis process. The rest of this paper is organized as the follows. Section 2 describes the model and experiment designs. Section 3 describes various sensitivity experiments, introduces a genesis efficiency index, and examines the dynamic and thermodynamic structure changes associated with mid-level and low-level precursors. A further discussion of the relative roles of surface fluxes and planetary boundary layer (PBL) processes and the oscillatory behavior of the relative humidity is given in Section 4. Finally, a conclusion is given in Section 5.

2. Model and experimental design

The results presented in this paper are based on a series of idealized numerical simulations. The cloud-resolving WRF-ARW model is used to simulate idealized EBV and EMV genesis events. The model is quadruply nested with two-way interaction. The mesh sizes in all four domains are 181×181 with horizontal grid sizes of 54, 18, 6, and 2 km, respectively. There are 27 levels in the vertical. The Kain-Fritch convective scheme is applied in the two outer meshes and an explicit microphysics scheme (Lin et al. 1983) is used in all four meshes. The PBL scheme follows Noh et al. (2003), which is an improved version of the Medium Range Forecast (MRF) scheme of Hong et al. (1996). Both longwave and shortwave radiation processes are included in the simulations. We used a fixed lateral boundary condition, that is, the tendency of prognostic variables in the lateral boundary is set to

be zero.

Table 1 lists all the experiments designed in this study. In each experiment, we specify a weak initial balanced axisymmetric vortex with a wind profile as follows:

$$V_t(r,\sigma) = A(\sigma)\frac{3\sqrt{6}}{4}\mathrm{V_m}\left(\frac{\mathrm{r}}{\mathrm{r_m}}\right)\left[1+\frac{1}{2}\left(\frac{\mathrm{r}}{r_m}\right)^2\right]^{-\frac{3}{2}}$$

where r is the radial distance from the vortex center, V_m the maximum tangential wind at the radius of r_m, σ is vertical sigma level, and $A(\sigma)$ is chosen to define the vertical structure. Given the wind fields, the mass and thermodynamic fields are then obtained based on a nonlinear balance equation so that the initial vortex satisfies both the hydrostatic and gradient wind balances.

In the first experiment (MID_VORTEX), we mimic a mid-level precursor condition, by specifying an initial cyclonic vortex that has maximum vorticity at 600 hPa. The horizontal structure of this mid-level vortex has a maximum wind speed of 8 m s^{-1} at a radius of 100 km and a size of 500 km radius (where the wind vanishes). The vorticity gradually decreases both upward and downward, and vanishes at the surface. In the second experiment (BTM_VORTEX), an initial maximum precursor perturbation with a maximum wind speed of 8 ms^{-1} is located at the surface. Figures 2a and 2b show the vertical-radial cross section of the tangential wind of these initial vortices. In both cases, the initial water vapor mixing ratio and other thermodynamic variables are assumed horizontally homogeneous and have the vertical profiles of typical January mean observations at Willis Island, northeast of Australia (Holland 1997). Other model parameter settings are identical to those described in Zhou and

Wang (2009). The model is set on an *f*-plane centered at 15^{o}N, and a quiescent environment with a constant sea surface temperature (SST) of 29^{o}C is specified.

The aforementioned two vortex vertical profiles are quite similar to the "surface vortex" and "mid-level vortex" cases in Nolan (2007). To investigate the dependence of TC genesis efficiency on initial vorticity and humidity profiles, three sensitivity experiments are further conducted to explore the impacts of the initial vorticity vertical structures (SHAL_MID and SHAL_BTM) and the initial moisture field (MOIST) on genesis efficiency. The details for these sensitivity experiments will be described in section 3.

3. Cyclogenesis efficiency and development characteristics

Starting from an initial weak vortex with a vertical profile described in Fig. 2, the model is integrated for 96 hours for all cases except for the "SHL_MID" case in which the model in integrated for 144 hours due to much slower cyclone development. In all experiments, the initial weak vortex develops into a mature TC. Figure 3 illustrates the final state of the simulated axisymmetric TC wind fields in MID_VORTEX. The simulated TC characteristics include a tilted eyewall, a vigorous in-up-and-out secondary circulation, and subsidence within the eyewall. The maximum tangential wind speed reaches 60 ms^{-1} at a radius of about 20 km. Strong inflow appears in the PBL, with maximum inflow just outside the radius of the maximum tangential wind. A broad outflow layer appears in the upper troposphere outside the eyewall. The final state of the TCs simulated in the other cases is generally

similar to that shown in Fig. 3.

The time evolutions of the minimum sea level pressure (MSLP) simulated from the four sensitivity experiments are shown in Fig. 4a. A marked difference among these experiments is the timing of a rapid pressure drop, suggesting that each genesis event possesses distinct genesis efficiency. Hereby we define the genesis time of each run as time when the maximum surface wind reaches 17.5 ms^{-1} (a criterion for the tropical storm strength). Figure 4b shows the time evolutions of the corresponding maximum surface wind speed from the four experiments. Based on the definition above, the genesis time occurs at hour 33 for BTM_VORTEX, hour 66 for MID_VORTEX, hour 78 for SHAL_BTM, and hour 114 for SHAL_MID, respectively.

Before discussing genesis efficiency differences among the experiments, we first examine their structure evolution characteristics. Figure 5 presents the vertical cross section of the relative vorticity and temperature anomaly fields averaged over the vortex core region (a box of 100 km by 100 km centered on the MSLP) from the four experiments. Here the temperature anomaly is defined as departure from the mean temperature over the innermost domain. Because the MSLP center in the first few hours is not well defined, for simplicity during that period we use the environmental vortex center instead. Once the surface pressure anomaly becomes well defined, we use the MSLP as the center for averaging. This method follows Montgomery et al. (2006).

In MID_VORTEX, the initial mid-level vorticity maximum coincides well with

a cold (warm) core below (above) 600 hPa (top left panel of Fig. 5), due to the thermal wind relationship. During the first 30 hours, the mid-level cyclonic vorticity gradually weakens and the “cold core” structure becomes less distinct. The mid-level vortex re-intensifies and creates a maximum vorticity center at 500 hPa at hour 48. Associated with this re-establishment of the mid-level vortex is the development of a cold-warm-core couplet and the mid-level convergence. The temperature anomaly shows a clear cold (warm) anomaly below (above) 600 hPa. Weak divergence appears around 800 hPa before hour 60, implying descending motions and a relative dry layer between 600 and 800 hPa. The thermodynamic structure at hours 48-60 bears the typical characteristics of stratiform precipitation regime (Yuter and Houze 1995), indicating that stratiform cloud is dominated at this time.

The similar plots for BTM_VORTEX are depicted in the bottom left panel of Fig. 5 for comparison. In this case, a rapid pressure drop occurs after hour 33, indicating a faster vortex development compared to MID_VORTEX. Although initially the maximum vorticity appears at the low levels, a mid-level vorticity enhancement is observed at hour 30. Associated with this mid-level vorticity enhancement is a cold-warm-core couplet (i.e., a cold core at lower level and a warm core above, bottom left panel of Fig. 5). The temperature and vorticity profiles at that time are associated with a mid-level convergence and downdrafts below, reflecting stratiform cloud regime. Although the development rate is slower in the two shallow vortex cases, the vorticity and temperature evolution characteristics in SHAL_MID and SHAL_BTM (right panels of Fig. 5) bear many similarities to their counterparts.

A common feature among the EBV and EMV experiments is the formation of a mid-level maximum vorticity prior to TC genesis irrespective where the initial vorticity maximum locates. A comparison of the BTM_VORTEX and MID_VORTEX experiments indicates that the former has greater genesis efficiency. A possible cause of this genesis efficiency difference is attributed to the initial column integrated absolute vorticity. Physically, it is argued that a vertically integrated environmental absolute vorticity may affect vorticity segregation (Schecter and Dubin 1999) or VHT merging. It may also affect the inertial stability and hence the efficiency of a transfer of latent heat to kinetic energy (Hack and Schubert 1986). Our calculations of column-integrated (from 1000hPa to 200hPa) absolute vorticity (averaged within a radius of 200 km) show that the integrated absolute vorticity in BTM_VORTEX ($3.98\text{x}10^{-5}\text{s}^{-1}$) is indeed greater than that in MID_VORTEX ($2.15\text{x}10^{-5}\text{s}^{-1}$), because the former has a deeper vertical structure than the latter (Fig. 2). Thus the numerical simulations support the notion that the larger initial column integrated absolute vorticity, the greater cyclogenesis efficiency is.

Another factor accounting for the genesis efficiency difference is the initial wind field in PBL. For example, cyclonic vorticity at top of PBL may induce boundary layer convergence, which further affects low-level vorticity generation through vorticity stretching (Chen and Frank 1993; Montgomery et al. 2006; Tory et al. 2006a) and boundary layer moisture through moisture convergence. The PBL wind may directly affect the surface latent heat fluxes and thus PBL moisture. The effect of the PBL moisture convergence is assessed by calculating the term $-\nabla\cdot(uq, vq)$. To

examine the large-scale feature, we apply a spatial filter technique to filter out the VHT-scale (wavelength less than 20 km) component. The result shows that prior to hour 24, BTM_VORTEX exhibits greater PBL moisture convergence than MID_VORTEX (figure not shown). The stronger PBL moisture convergence favors a more convectively unstable stratification, leading to enhanced VHT activity. Our vorticity budget analysis shows that compared to the MID_VORTEX case, the stronger low-level convergence in BTM_VORTEX leads to greater vorticity generation through vorticity stretching.

To clearly demonstrate the PBL effect, two sensitivity experiments named SHAL_MID and SHAL_BTM are further conducted. Figures 2c and 2d show the vertical-radial cross section of the tangential winds of these two initial vortices. In SHAL_MID, the initial mid-level vortex is similar to that in MID_VORTEX except confined to a shallower layer. That is, the wind speed associated with the mid-level vortex vanishes below the 800 hPa level. In SHAL_BTM, the initial vortex profile is similar to BTM_VORTEX except that the circulation is mainly confined within the PBL (i.e., the wind speed vanishes above 800 hPa). The two initial vortices have quite similar vertically (1000hPa - 200hPa) integrated absolute vorticity ($1.46 \times 10^{-5} s^{-1}$ in SHAL_BTM versus $1.68 \times 10^{-5} s^{-1}$ in SHAL_MID).

Given the similar column integrated vorticity, the genesis efficiency is quite different between SHAL_BTM and SHAL_MID (Fig. 4). The genesis occurs at hour 78 in SHAL_BTM, which is much faster than that in SHAL_MID (at hour 114). This suggests that besides the column integrated absolute vorticity, other factors must play

a role in determining the genesis efficiency.

An obvious difference between SHAL_BTM and SHAL_MID lies in the PBL wind profile. Compared to SHAL_MID, SHAL_BTM has an initial vortex structure that favors greater surface fluxes due to greater surface wind speed and greater PBL moisture convergence due to Ekman-pumping induced boundary layer convergence. These processes lead to a marked difference in the PBL humidity during the initial development stage, which may help set up more quickly a convectively unstable stratification and enhance VHT activity. A comparison between SHAL_BTM and SHAL_MID confirms that there are indeed more and stronger VHTs in SHAL_BTM during the first 24 hours.

The experiments above suggest that besides the column integrated absolute vorticity, the PBL wind profile may also affect genesis efficiency. Both the factors above are related to the dynamic part of the environmental conditions. In addition, the initial relative humidity profile may also affect genesis efficiency. To demonstrate this, we conducted an additional sensitivity experiment (named MOIST), in which the identical model setting as that in MID_VORTEX is used except with a higher initial relative humidity condition (see Fig. 6a for the new RH profile). The initial RH increases by 8% at the surface and 50% at 500 hPa. Figures 6b and 6c present the vertical cross sections of the relative vorticity and temperature anomaly fields averaged over the core region (i.e., a 100 km by 100km box) in MOIST. Similar to MID_VORTEX, the mid-level vorticity weakens initially, but it quickly develops into a TC within a 24-hour period, indicating greater genesis efficiency compared to

MID_VORTEX. A rapid intensification of low-level vorticity occurs after hour 18, along with strong low-level convergence. Associated with these changes, the surface central minimum pressure drops rapidly (Fig. 6d). Because the environment is nearly saturated from the boundary layer up to the middle troposphere, less evaporative cooling of raindrops leads to a more rapid increase in the low-level vorticity through vortex stretching.

A common development characteristic among the five experiments above is the occurrence of upscale cascade from cumulus-scale (~ 5km) VHTs to a meso-vortex-scale (~ 50-100 km) system (MVS). Figure 7 illustrates this upscale cascade process based on the evolution of the low-level wind and vorticity fields in MID_VORTEX and BTM_VORTEX. In both cases, sporadic cumulus-scale (~5 km) convective cells develop shortly after the model initialization, due to the conditionally unstable environmental thermal condition and the surface latent heat flux. A vertical cross section through a typical updraft convective cell shows that the cell is quite deep, with strong cyclonic vorticity extending from the near surface to 400 hPa. While the cumulus-scale (~5 km) VHTs are randomly triggered, they are gradually organized and merged into a MVS through merging around the environmental vorticity center. This warm-core MVS differs from conventional mid-latitude mesoscale convective systems that have a distinct cold-core structure. As shown in Fig. 7, in MID_VORTEX, several convective cells move closer and merge into a larger vortex with a horizontal scale of about 50 km at 48 hour. A similar evolution feature is identified in BTM_VORTEX, although cumulus-scale VHTs and a MVS develop

earlier than MID_VORTEX.

Vorticity segregation (Schecter and Dubin 1999) is a possible mechanism for the VHTs merging. That is, cyclonic (anticyclonic) vorticity anomalies move up (down) the ambient vorticity gradient. As a result, cyclonic vorticity anomalies tend to move inward toward the vortex centre, while anticyclonic anomalies tend to move outward away from the centre. This vorticity segregation as well as vortex merger and axisymmetrization (Montgomery et al. 2006) may cause upscale cascade from cumulus-scale (~5 km) VHTs to a MVS. As seen from all five experiments, this upscale cascade is the first key step toward the cyclogenesis. A related mechanism is the so-called system-scale intensification (SSI, Montgomery et al. 2006; Tory et al. 2006b). On one hand, the VHTs provide seed vorticity that contributes to vortex upscale cascade; on the other hand, the net heating from these convective updrafts drives the transverse circulation necessary for the spin up of the azimuthal mean vortex. The convergent inflow helps the VHTs move inward, resulting in a single but more intense vorticity anomaly. A 50km core vortex is absent at hour 12 (24) but is clearly present at hour 24 (48) in BTM_VORTEX (MID_VORTEX) (Fig. 7). The core will eventually evolve into a TC. Once the MVS system forms, the adjacent convective cells will be further absorbed, or organized into outer spiral rainbands (Kuo et al. 2004). During the upscale cascade process, the surface wind speed is strengthened, which will further strengthen the MVS system through increased surface evaporation and moisture.

The strength of the VHTs at a given time may be measured by counting the grid

points over which 850hPa relative vorticity exceeds a threshold value (i.e., $3x10^{-4}$ s^{-1}). For a fixed domain of 180km x 180km (shown in Fig. 7), one may calculate the percentage of the area that exceeds the vorticity threshold. (Different from the previous emphasis in the vortex core region, here we use a larger domain in an attempt to include initial randomly-generated VHT-like systems that spread in a relatively larger area.) Figure 8 shows the time evolution of the VHT percentage area. It is interesting to note that, among the five experiments, the VHT activity is most active in MOIST and least active in SHAL_MID. Physically this is reasonable because greater initial humidity in MOIST leads to a quicker setup of the convectively unstable stratification and thus the VHT development, while the lack of PBL moisture convergence and weaker surface fluxes in SHAL_MID lead to a slower setup of the convectively unstable stratification and thus weaker VHT activity. In general, the rate of the VHT area increase is consistent with the genesis time for the five experiments above.

A salient feature is a close relationship between the setup of a deep moist layer and TC genesis. For instance, in MID_VORTEX (Fig. 9a), there is a steady increase of the moist layer in the core region during hours 24-60. The "90%" RH layer (shaded in Fig. 9a) thickens from 900 hPa at hour 24 to about 500 hPa at hour 60. The establishment of this near-saturated air column signifies the next development stage: a rapid drop of minimum sea level pressure (as seen in Fig. 4). A similar deepening of the moist layer (represented by 90% RH contour) from the PBL to 500 hPa appears at hours 12-30 in BTM_VORTEX (Fig. 9b), hours 72-108 in SHAL_MID (Fig. 9c),

hours 36-66 in SHAL_BTM (Fig. 9d), and hours 0-12 in MOIST (Fig. 9e).

In the five experiments above, the genesis time occurs shortly after a near-saturated air column is set up. This preconditioning of the deep moist layer in the core region was suggested by Bister and Emanuel (1997) and confirmed with numerical experiments by Nolan (2007). Figure 10 further illustrates the evolution of the vertically (1000hPa-500hPa) integrated RH averaged in the core region and its relationship with the TC genesis. Note that cyclogenesis starts in the all five experiments shortly after the column averaged RH reaches 90%. This confirms that the establishment of a near-saturated air column is indeed a precondition for cyclogenesis.

The five experiments above demonstrate the important roles of initial wind and humidity profiles in determining genesis efficiency. This motivates us to define an index to quantitatively measure the dependence of the genesis efficiency on initial environmental dynamic and thermodynamic conditions. Following the formula of Emanuel and Nolan (2004) and considering the aforementioned simulation results, we introduce a genesis efficiency index (GEI) under a warm-pool no-shear environment as:

$$GEI = \left|10^5 \times \bar{\eta}\right|^{3/2} \left(\frac{\overline{RH}}{50}\right)^3 \max(0.1, \frac{\varsigma_{850}}{f_0})$$

where $\bar{\eta}$ denotes the initial vertically integrated absolute vorticity averaged within a radius of 200 km from the surface to 200hPa, $\overline{RH}$ is the initial column averaged RH (from the surface to 500hPa), and ς_{850} and f_0 are initial environmental relative vorticity at 850 hPa and Coriolis parameter, respectively. We choose $\overline{RH}$ rather than

a single level such as 700 hPa *RH* to emphasize the importance of establishment of a near-saturated air column in TC genesis. Furthermore, $\frac{\zeta_{850}}{f_0}$ represents non-dimensional 850hPa relative vorticity to measure the strength of Ekman-pumping induced PBL convergence. A minimum non-dimensional 850hPa environmental vorticity (0.1) is given to avoid a "null" value in SHAL_MID.

Figure 11 illustrates the relationship between the model genesis time and the calculated GEI. The index reflects well the impact of the initial environmental vorticity and moisture profiles on genesis efficiency. That is, a larger GEI corresponds to a faster genesis period. For instance, MOIST has the highest GEI and the shortest genesis period, indicating the important role of setup of a near-saturated air column in TC genesis. In SHAL_MID, the GEI is the smallest, corresponding to the slowest cyclone development. The GEI is greater in SHAL_BTM than in SHAL_MID, because the former attains greater PBL convergence even though it has slightly weaker initial column integrated absolute vorticity.

4. Discussion

While the comparison of SHAL_BTM and SHAL_MID clearly demonstrates the role of the PBL, the relative roles of boundary layer convergence and surface fluxes in affecting cyclogenesis is not clear. To clarify this issue, two additional sensitivity experiments (named SHAL_BTM8 and SHAL_MID8) were conducted. In SHAL_BTM8 (SHAL_MID8), the initial condition is the same as that in SHAL_BTM (SHAL_MID), except that a constant surface wind speed was given

throughout the model integration (i.e., $|V_{10}|$=8 ms^{-1}) when the surface heat fluxes were calculated. By doing so, we minimize the differences due to the surface fluxes in SHAL_BTM and SHAL_MID so that we may examine the sole PBL convergence effect.

Figure 12 shows the time evolutions of the maximum surface wind speed in the two experiments. For comparison, the evolutions of the maximum surface wind speed in SHAL_BTM and SHAL_MID are also plotted here. Due to artificially enhanced surface fluxes during the initial period in SHAL_MID8, the genesis time shortens markedly (about 30 hours) compared to that in SHAL_MID. This suggests that the enhanced surface fluxes favor greater VHT activity and thus faster intensification. The diagnosis of the model output confirms that the initially enhanced surface fluxes indeed lead to more vigorous VHT activity in SHAL_MID8 than in SHAL_MID. In contrast, the change of the genesis time from SHAL_BTM8 to SHAL_BTM is minor, due to the relatively small increase of the surface wind speed during the initial development stage. The difference of the genesis time (about 12 hours) between SHAL_MID8 and SHAL_BTM8 reflects the pure effect of the PBL convergence, because the surface fluxes are quite similar in the two experiments. Thus, the additional sensitivity experiments indicate that both the surface fluxes and the PBL convergence are crucial in determining the genesis efficiency difference between the mid-level and bottom vortex cases.

Why does the initial vorticity profile matter? We argue that the environmental mid-level or bottom cyclonic vorticity provides an important background source to

trigger and organize randomly generated cloud or VHT cells. These convective cells or VHTs are organized and merged into a warm-cored MVS through vortex upscale cascade and SSI processes. The MVS has longer life duration and a larger horizontal scale than any individual VHTs and can serve as a core for the sustained development of a TC.

As seen from Fig. 10, the column integrated RH in the core region exhibits an oscillatory development characteristic. What causes such an oscillation? We argued that the RH oscillation is related to the convective-stratiform phase transition. The top panels of Fig. 13 show the vertical-time sections of the latent heating rate averaged over the vortex core region in MID_VORTEX and BTM_VORTEX. The latent heating clearly reveals a convective-stratiform phase transition. For instance, in MID_VORTEX, a rapid increase of the latent heating rate appears at hours 30-36, reflecting the enhanced convective activity in the core region. Thereafter, the positive diabatic heating center gradually shifts to the upper troposphere, while a negative heating center (attributed to raindrop induced evaporative cooling) appears in the lower troposphere. Such a vertical heating profile at hour 48 represents a typical stratiform cloud regime with a weak heating (cooling) being aloft (below) the freezing level (Houze 1993). After hour 60, the heating rate increases dramatically, indicating a new phase of the convective development in the core region.

The oscillatory behavior is likely attributed to the discharge and recharge of the atmospheric convective instability, as first pointed out by Li et al. (2006). The bottom panels of Fig. 13 illustrate the time-vertical cross section of the equivalent potential

temperature (θ_e) and $\Delta\theta_e$ (defined as the difference of θ_e between 900 and 700hPa) averaged over the core region. When $\Delta\theta_e$ increases (decreases), the atmosphere becomes more convectively unstable (stable). In MID_VORTEX, the value of $\Delta\theta_e$ increases during hour 36-54, suggesting the recharging of the convective instability in that period. The atmosphere becomes stable after the convective bursts occur. Thus the convective instability is accumulated (consumed) during the stratiform (convective) phase. This characteristic appears in BTM_VORTEX as well (e.g., at hours 24-30). At this stratiform phase, the evaporative cooling and melting associated with the precipitation and/or the falling ice particles induce downdrafts, which bring dry air downward to cause the mid-level dryness.

The simulated stratiform-convective phase oscillation feature is consistent with previous observational and modeling studies (e.g., Zehr 1992; Li et al. 2006; Lee et al. 2008). While the mesoscale deep convection brings the moisture upward and thus contributes to the deepening of a moist layer in the core region, it can only be sustained for a few hours due to its natural life cycle. As the deep convection ceases, the vortex core experiences a stratiform cloud phase characterized by the occurrence of a mid-level vorticity maximum and a thermal cold-warm-core couplet. The downdrafts associated with the raindrop-induced evaporative cooling enhance the mid-level minimum of θ_e. The reduction of mid-level θ_e, along with the recharge of PBL moisture due to surface evaporation, leads to the re-establishment of a convectively unstable stratification and thus triggers a new deep convective phase. The new convective bursts continue to moisten the air column while enhancing the

low-level vorticity. This explains why the vertically integrated RH shows an oscillatory development feature.

It is worth mentioning that the current formula of the genesis efficiency index does not include environmental conditions related to vertical wind shear and SST. A further refining of the index is needed based on either cloud-resolving model simulations or observations, with more environmental parameters to be considered.

5. Conclusion

A cloud-resolving WRF model is used to simulate TC genesis events in an environment with a near bottom vortex (EBV) and an environment with a mid-level vortex (EMV). The sensitivity experiments show that the timing of the TC genesis is sensitive to initial vorticity and moisture profiles. The greater initial column integrated absolute vorticity, the faster the cyclogenesis is. For given the same column integrated absolute vorticity, a bottom vortex has higher cyclogenesis efficiency than a mid-level vortex.

A common feature among the EBV and EMV experiments is the emergence (or re-emergence) of a mid-level vortex prior to rapid TC development no matter whether the initial vorticity maximum is located at the mid level or at the bottom. The exact cause of the emergence or re-emergence is not clear at the moment. It is likely attributed to the TC oscillatory development associated with the phase transition from a convective (stratiform) to a stratiform (convective) phase as suggested by Li et al. (2006). The numerical simulations point out that an enhanced bottom vortex and an

enhanced mid-level vortex may occur during the different stages of the same TC genesis event.

It is noted that the EBV and EMV scenarios share the following development characteristics: 1) a transition from non-organized cumulus-scale (~5 km) convective cells or VHTs to an organized surface concentrated meso-vortex-scale (~50-100km) system (MVS); 2) a multiple stratiform-convective phase oscillation; and 3) a setup of a near-saturated meso-vortex-scale air column prior to a rapid pressure drop.

Following the formula of the genesis potential index by Emanuel and Nolan (2004), we introduce a genesis efficiency index (GEI) to reflect the impact of initial wind and moisture profiles on cyclogenesis. The key parameters in the GEI include the column integrated (1000hPa-200hPa) absolute vorticity, vorticity at top of the PBL, and vertically integrated (1000hPa-500hPa) relative humidity. Our calculations show that the GEI reflects well the model simulated genesis efficiency feature.

Compared to previous simulations (e.g., Hendricks et al. 2004; Montgomery et al. 2006; Nolan et al. 2007; and many others), the route to genesis is generally similar. For instance, a transition from non-organized cumulus-scale (~ 5km) convective cells into an organized surface-concentrated meso-vortex-scale (~50-100 km) system through upscale cascade or SSI is a common process among these models. Here we suggest that a multiple convective-stratiform-convective phase transition is a necessary route to set up a deep moist layer. The phase oscillation, however, may be sensitive to the model microphysics scheme. In a model lacking significant stratiform dynamics, this stage might not be well represented. Therefore, it would be interesting

to compare the oscillatory feature in various models with different microphysics schemes. Furthermore, it is unclear whether the setup of a near-saturated air column is necessary for cyclogenesis under a sheared environment, which deserves further observational and modeling studies.

Acknowledgement. The authors would like to thank Drs. Kevin Tory and Zhuo Wang for their valuable comments and suggestions. This work was supported by ONR Grants N000140810256 and N000141010774 and by International Pacific Research Center that is partially sponsored by the Japan Agency for Marine-Earth Science and Technology (JAMSTEC), NASA (NNX07AG53G) and NOAA (NA17RJ1230). This is SOEST contribution number xxxx and IPRC contribution number xxx.

Reference

Bister, M., and K. A. Emanuel, 1997: The genesis of Hurricane Guillermo: TEXMEX analyses and a modeling study. Mon. Wea. Rev., 125, 2662-2682.

Bosart, L. F. and F. Sanders, 1981: The Johnstown flood of July 1977: A long-lived convective system. J. Atmos. Sci., 38, 1616-1642.

Chang, C.-P., V. F. Morris, and J. M. Wallace, 1970: A statistical study of easterly waves in the western Pacific: July–December 1964. J. Atmos. Sci., 27, 195–201.

Chang, C.-P., J. M. Chen, P. A. Harr, and L. E. Carr, 1996: Northwestward-propagating wave patterns over the tropical western North Pacific during summer. Mon. Wea. Rev., 124, 2245–2266.

Chen, S. S. and W. M. Frank, 1993: A numerical study of the genesis of extratropical convective mesovortices. Part I: Evolution and dynamics. J. Atmos. Sci., 50, 2401–2426.

Emanuel, K., and D. S. Nolan, 2004: Tropical cyclone activity and the global climate system. 26th Conference on Hurricanes and Tropical Meteorology, Am. Meteorol. Soc., Miami, FL.

Fu, B., T. Li, M.S. Peng, and F. Weng, 2007: Analysis of tropical cyclogenesis in the western North Pacific for 2000 and 2001. Weather and Forecasting, 22, 763–780.

Ge, X., T. Li, and M.S. Peng, 2010: Cyclogenesis simulation of Typhoon Prapiroon (2000) associated with Rossby wave energy dispersion. Mon. Wea. Rev., 138, 42-54.

Hack, J.J., and W.H. Schubert, 1986: Nonlinear response of atmospheric vortices to

heating by organized cumulus convection. J. Atmos. Sci., 43, 1559-1573.

Hendricks, E. A., M. T. Montgomery, and C. A. Davis, 2004: The role of vortical hot towers in the formation of Tropical Cyclone Diana (1984). J. Atmos. Sci., 61, 1209–1232.

Holland, G. J., 1995: Scale interaction in the western Pacific monsoon. Meteor. Atmos. Phys., 56, 57–79.

Holland, G. J., 1997: The maximum potential intensity of tropical cyclones. *J. Atmos. Sci.*, **54,** 2519–2541.

Hong, S.-Y., and H.-L. Pan, 1996: Nonlocal boundary layer vertical diffusion in a Medium-Range Forecast model. Mon. Wea. Rev., 124, 2322-2339.

Houze, R. A., Jr., 1993: *Cloud Dynamics*. Academic Press, San Diego, 573 pp.

Houze, R. A., Jr., W.-C. Lee, and M. M. Bell, 2009: Convective Contribution to the Genesis of Hurricane Ophelia (2005). Mon. Wea. Rev., 137, 2778–2800.

Kuo, H.-C., L.-Y. Lin, C.-P. Chang, and R. T. Williams, 2004: The formation of concentric vorticity structure in typhoon. J. Atmos. Sci., 61, 2722-2734.

Lau, K.-H., and N.-C. Lau, 1990: Observed structure and propagation characteristics of tropical summertime synoptic-scale disturbances. Mon. Wea. Rev., 118, 1888–1913.

Lee, C. -S., K. -W. Cheung, J. -N. Hui, R. L. Elsberry, 2008: Mesoscale features associated with tropical cyclone formations in the Western North Pacific. Mon. Wea. Rev., 136, 2006–2022.

Li, T., B. Fu, X. Ge, B. Wang, and M. Peng, 2003: Satellite data analysis and

numerical simulation of tropical cyclone formation. Geophys. Res. Lett., 30 (21), 2122, doi:10.1029/2003GL018556.

Li, T., and B. Fu, 2006: Tropical cyclogenesis associated with Rossby wave energy dispersion of a preexisting typhoon. Part I: Satellite data analyses. J. Atmos. Sci., 63, 1377–1389.

Li, T. X. Ge, B. Wang, and T. Zhu, 2006: Tropical cyclogenesis associated with Rossby wave energy dispersion of a pre-existing Typhoon. Part II: numerical simulations. J. Atmos. Sci., 63, 1390-1409.

Lin, Y.-L., R. D. Rarley, and H. D. Orville, 1983: Bulk parameterization of the snow field in a cloud model. J. Appl. Meteor., 22, 1065-1092.

Montgomery, M. T., M. E. Nicholls, T. A. Cram, and A. B. Saunders, 2006: A vortical hot tower route to tropical cyclogenesis. J. Atmos. Sci., 63, 355-386.

Noh, Y., W. G. Cheon, S. Y. Hong, and S. Raasch, 2003: Improvement of the K-profile model for the planetary boundary layer based on large eddy simulation data. Bound.-Layer Meteor., 107, 401-427.

Nolan, D. S., 2007: What is the trigger for tropical cyclogenesis? *Aust. Meteorol. Mag.*, *56*, 241-266.

Nolan, D. S., Y. Moon, and D. P. Stern, 2007: Tropical cyclone intensification from asymmetric convection: Energetics and efficiency. *J. Atmos. Sci.* , *64* , 3377-3405.

Reasor, P. D., M. T. Montgomery, and L. F. Bosart, 2005: Mesoscale observations of the genesis of Hurricane Dolly (1996). J. Atmos. Sci., 62, 3151-3171.

Ritchie, E. A. and G. J. Holland, 1997: Scale interactions during the formation of Typhoon Irving. Mon. Wea. Rev., 125, 1377-1396.

Rogers, R. F., and J. M. Fritsch, 2001: Surface cyclogenesis from convectively driven amplification of midlevel mesoscale convective vortices, Mon. Wea. Rev., 129, 605– 637.

Schecter, D. A. and D. H. Dubin, 1999: Vortex motion driven by a background vorticity gradient. Phys. Rev. Lett., 83, 2191–2194.

Simpson, J., E. Ritchie, G. J. Holland, J. Halverson, and S. Stewart, 1997: Mesoscale interactions in tropical cyclone genesis. Mon. Wea. Rev., 125, 2643-2661.

Tam, C.-Y., and T. Li, 2006: The origin and dispersion characteristics of the observed summertime synoptic-scale waves over the western Pacific. Mon.Wea.Rev., 134, 1630-1646.

Tory, K. J., M. T. Montgomery, and N. E. Davidson, 2006a: Prediction and diagnosis of tropical cyclone formation in an NWP system. Part I: The critical role of vortex enhancement in deep convection. J. Atmos. Sci., 63, 3077-3090.

Tory, K. J., M. T. Montgomery, N. E. Davidson, and J. D. Kepert, 2006b: Prediction and diagnosis of tropical cyclone formation in an NWP system. Part II: A diagnosis of tropical cyclone Chris formation. J. Atmos. Sci., 63, 3091-3113.

Wang, Z., M. T. Montgomery, and T. J. Dunkerton, 2010: Genesis of Pre-hurricane Felix (2007). Part II: Warm core formation, precipitation evolution and predictability. J. Atmos. Sci., in press.

Yuter, S. E., and R. A. Houze, Jr., 1995: Three-dimensional kinematic and

microphysical evolution of Florida cumulonimbus. Part II: Frequency distribution of vertical velocity, reflectivity, and differential reflectivity. Mon. Wea. Rev., 123, 1941-1963.

Zehr, R., 1992: Tropical cyclogenesis in the Western North Pacific. NOAA Tech. Rep., NESDIS 61, 181 pp.

Zhang, D.-L., and J. M. Fritsch, 1987: Numerical simulation of the meso-beta-scale structure and evolution of the 1977 Johnstown flood. Part II: Inertially stable warm-core vortex and the mesoscale convective complex. J. Atmos. Sci., 44, 2593-2612.

Zhou, X., and B. Wang, 2009: From concentric eyewall to annular hurricane: A numerical study with the cloud-resolved WRF model. Geophys. Res. Lett., 36, L03802, doi:10.1029/2008GL036854.

Figure captions

Fig. 1 Left: Cloud liquid water content (g/kg) on August 6-8, 2001. The dot represents the TC Usagi genesis location. Right: surface QuikSCAT and 650hPa NCEP global final analysis wind fields, and the vertical profile of temperature anomaly (dashed line; K) and relative vorticity (solid line; $1\times10^{-4}s^{-1}$) averaged in the box area on 7 August, 2001.

Fig. 2 The vertical-radial cross section of the tangential wind of the initial vortex in MID_VORTEX (top) and BTM_VORTEX (bottom). Horizontal (vertical) axis is km (hPa).

Fig. 3 The azimuthally mean component of the simulated TC at t=96hr in MID_VORTEX: (a) tangential wind (contour) and vertical motion (shaded); (b) radial flow (unit: ms^{-1}). The vertical (horizontal) axis is (hPa) km.

Fig. 4 Time evolution of MSLP (top) and the maximum surface wind speed (bottom) in BTM_VORTEX (solid line), MID_VORTEX (dashed line), SHAL_BTM (dot-dashed line) and SHAL_MID (dotted line).

Fig. 5 Time-vertical pressure level (hPa) cross section of relative vorticity (1×10^{-5} s^{-1}) and temperature anomaly (°C) averaged over a 100 km×100km box centered at the MSLP in each experiment. Shading highlights large relative vorticity area, closely following vorticity contours.

Fig. 6 (a) The environmental relative humidity (%) profile used in MID_VORTEX (dashed line) and MOIST (solid line). (b-d) Time-vertical pressure level (hPa) cross section of mean values of inner-core variables averaged over a

100km×100km box for (b) relative vorticity (1×10^{-5} s^{-1}), (c) temperature anomaly (°C), and (d) MSLP (hPa) (MID_VORTEX: dashed line, MOIST: solid line). Shading highlights large relative vorticity area, closely following vorticity contours.

Fig. 7 The horizontal pattern of low-level (900hPa) wind field (vector) and relative vorticity (greater than $3\times10^{-4}s^{-1}$ are shaded) in MID_VORTEX (left) and BTM_VORTEX (right).

Fig. 8 The ratio of area of relative vorticity greater than 3×10^{-4} s^{-1} in a 180km by 180 km domain in MOIST (thin solid line), BTM_VORTEX (thick solid line), MID_VORTEX (dashed line), SHAL_BTM (dot-dashed line) and SHAL_MID (dotted line).

Fig. 9 Time-vertical pressure level (hPa) cross section of RH (%) averaged over a 100 km×100km box centered at the MSLP in each experiment. Shading highlights large relative humidity areas that exceed 90%.

Fig. 10 Time evolution of the column averaged $\overline{RH}$ (from the surface to 500hPa, averaged over a 100 km×100km box centered at the MSLP) in MOIST (solid line), BTM_VORTEX (long dashed line), MID_VORTEX (solid line with open circle), SHAL_BTM (dotted line with solid circle), SHAL_MID (solid line with open square), respectively. The hurricane symbols represent the genesis timing for each experiment. .

Fig. 11 The diagram shows the relationship of GEI to the genesis timing in the five experiments.

Fig. 12 The time evolution of maximum surface wind speeds in SHAL_BTM (thick solid line), SHAL_BTM8 (thin solid line), SHAL_MID (thick dashed line) and SHAL_MID8 (thin dashed line), respectively.

Fig. 13 Top: time-vertical cross section of latent heating rate (K/hr) averaged over a 100 km×100km box centered at the MSLP. Bottom: time-vertical cross section of θ_e (K) averaged over the same region and $\Delta\theta_e$ (defined as the difference of θ_e between 900 and 700hPa) in MID_VORTEX (left) and BTM_VORTEX (right). Different time periods are plotted in the horizontal axis for the two experiments.

Table 1 Model experiment description

Symbols	Experiments
MID_VORTEX	initial vortex with a mid-level maximum wind speed of 8 m s^{-1} at a radius of 100 km
BTM_VORTEX	initial vortex with a surface maximum wind speed of 8 m s^{-1} at a radius of 100 km
MOIST	same as MID_VORTEX except with higher initial relative humidity
SHAL_MID	similar to MID_VORTEX except with a shallower mid-level vortex (the wind vanishes below 800hPa)
SHAL_BTM	similar to BTM_VORTEX except the initial vortex is mainly confined below 800hPa
SHAL_MID8	Same as SHAL_MID except with a fixed surface wind speed of $8ms^{-1}$ in the surface heat flux calculation
SHAL_BTM8	Same as SHAL_BTM except with a fixed surface wind speed of $8ms^{-1}$ in the surface heat flux calculation

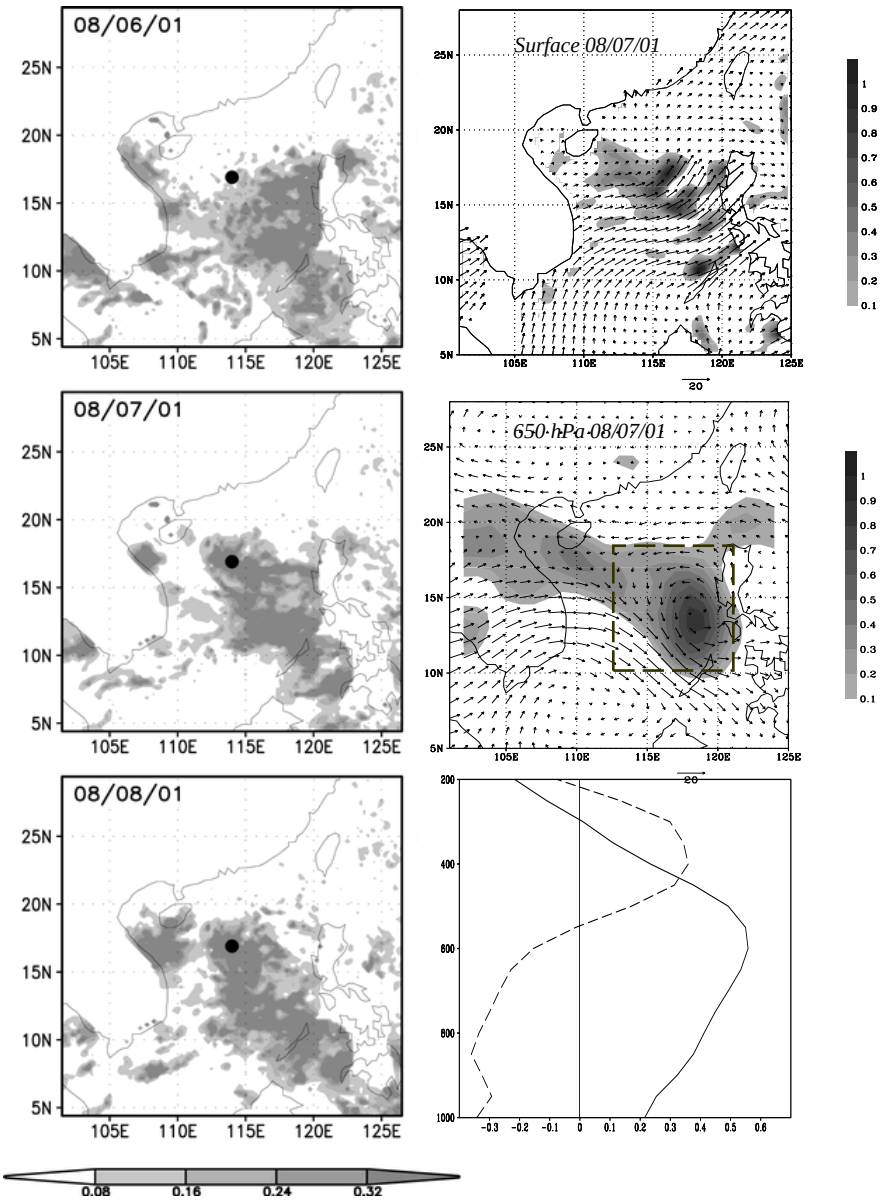

Fig. 1 Left: Cloud liquid water content (shaded; g/kg) on August 6-8, 2001. The dot represents the TC Usagi genesis location. Right: surface QuikSCAT (right-top panel) and 650hPa NCEP global final analysis wind fields (vector) and relative vorticity (shaded) (right-middle), and the vertical profile of temperature anomaly (dashed line; K) and relative vorticity (solid line; $1\times10^{-4}s^{-1}$) averaged in the box area on 7 August, 2001(right-bottom panel).

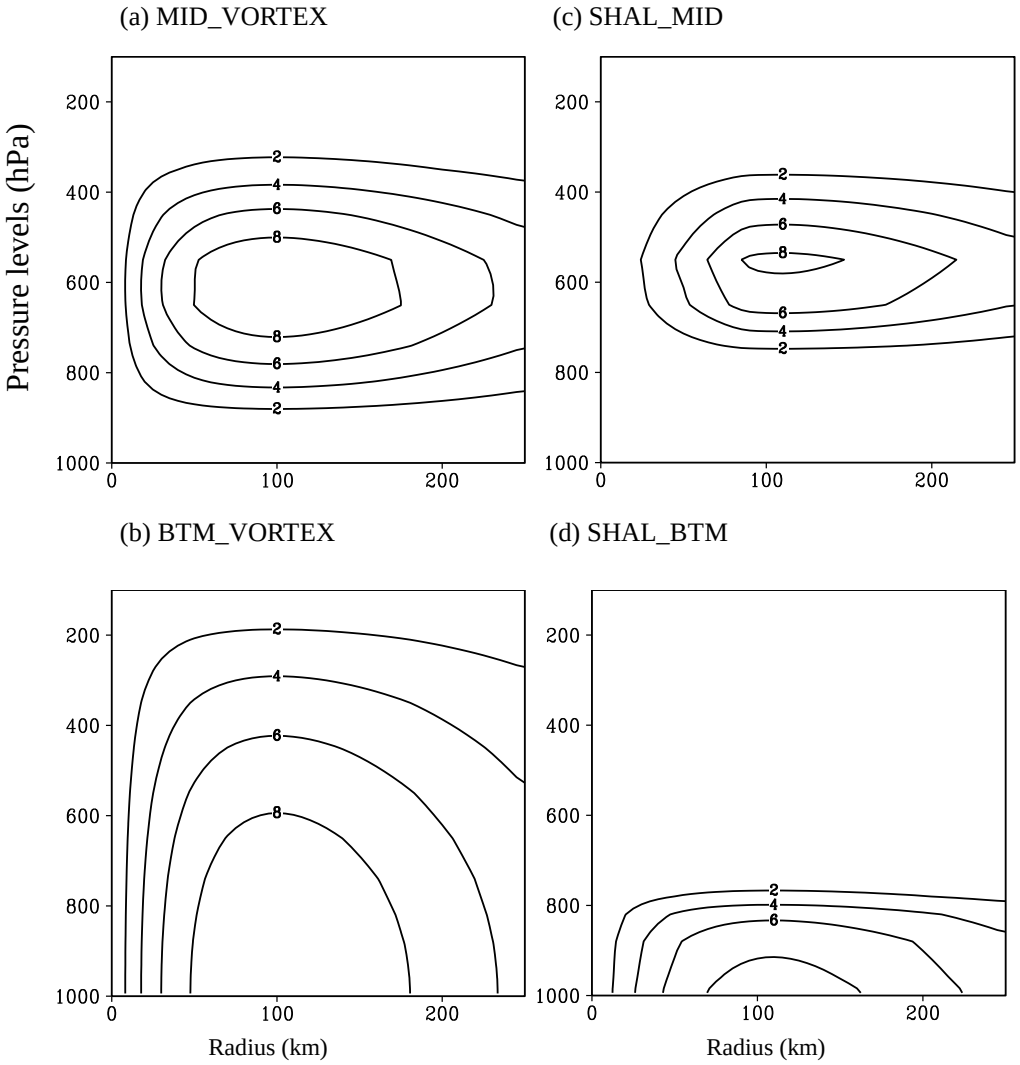

Fig. 2 The vertical-radial cross section of tangential velocity (ms^{-1}) of the initial vortex in (a) MID_VORTEX; (b) BTM_VORTEX; (c) SHAL_MID and (d) SHAL_BTM.

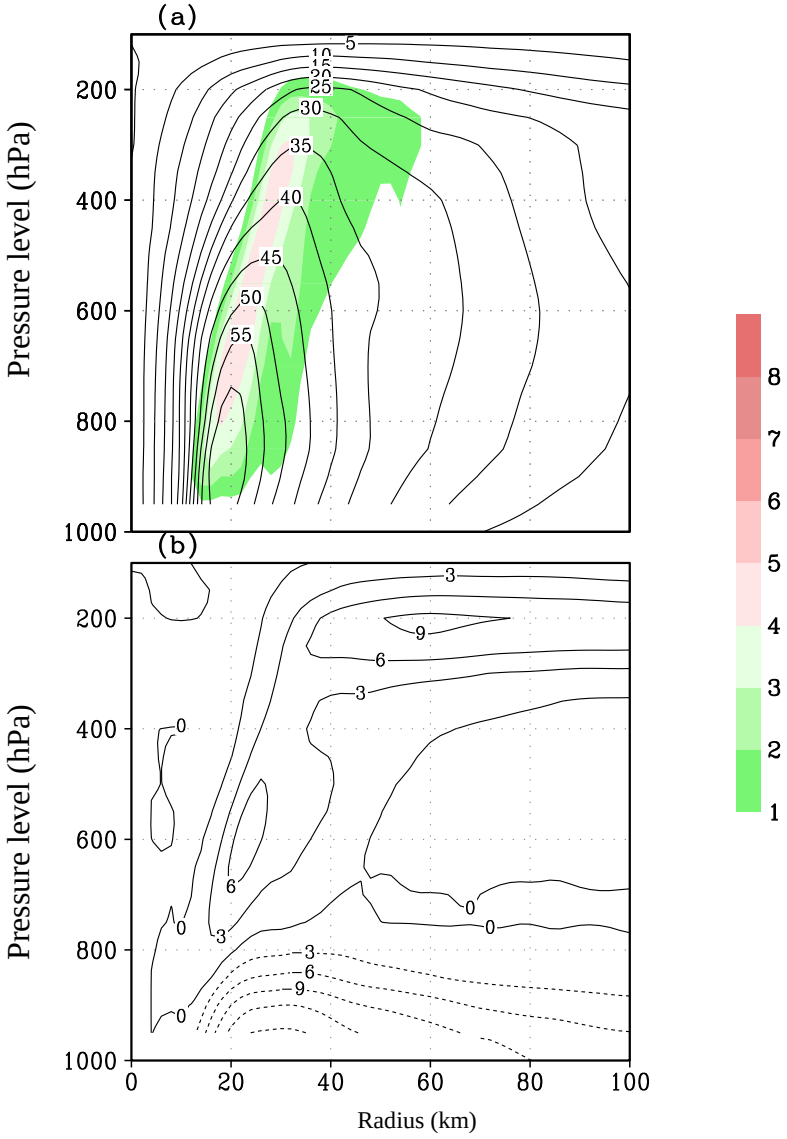

Fig. 3 The azimuthally mean component of the simulated TC in MID_VORTEX at t=96hr: (a) tangential wind (contour) and vertical motion (shaded); (b) radial flows. Unit: ms^{-1}.

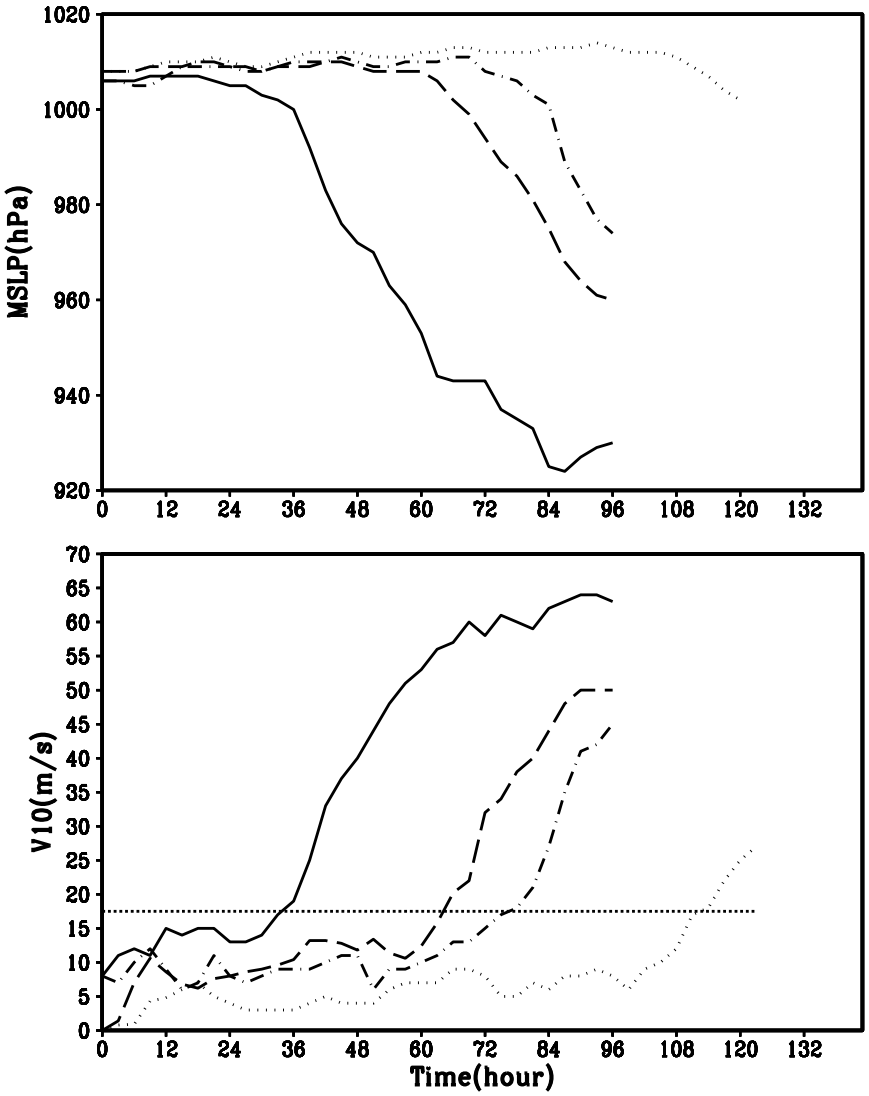

Fig. 4 Time evolution of MSLP (top) and the maximum surface wind speed (bottom) in BTM_VORTEX (solid line), MID_VORTEX (dashed line), SHAL_BTM (dot-dashed line) and SHAL_MID (dotted line).

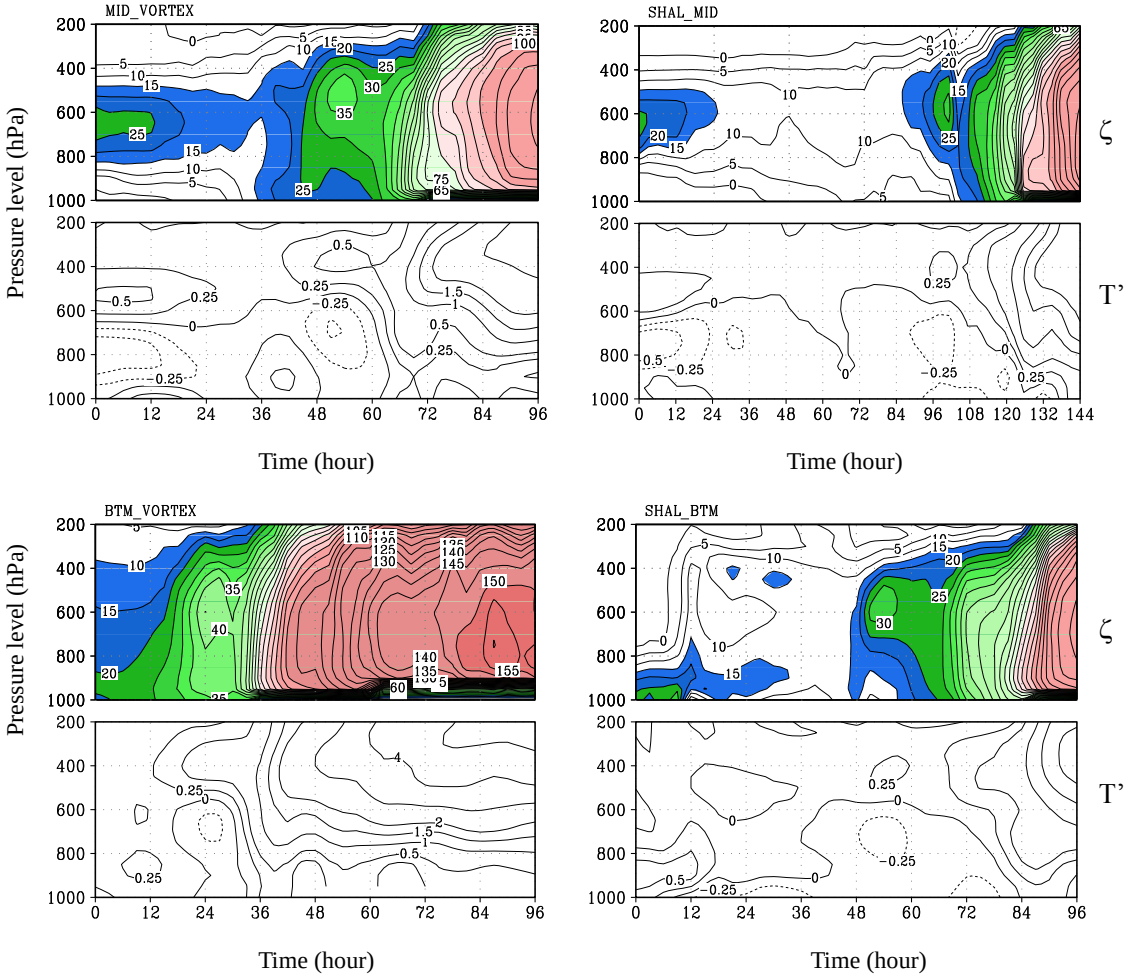

Fig. 5 Time-vertical pressure level (hPa) cross section of relative vorticity (1×10^{-5} s^{-1}) and temperature anomaly (°C) averaged over a 100 km×100km box centered at the MSLP in each experiment. Shading highlights large relative vorticity area, closely following vorticity contours.

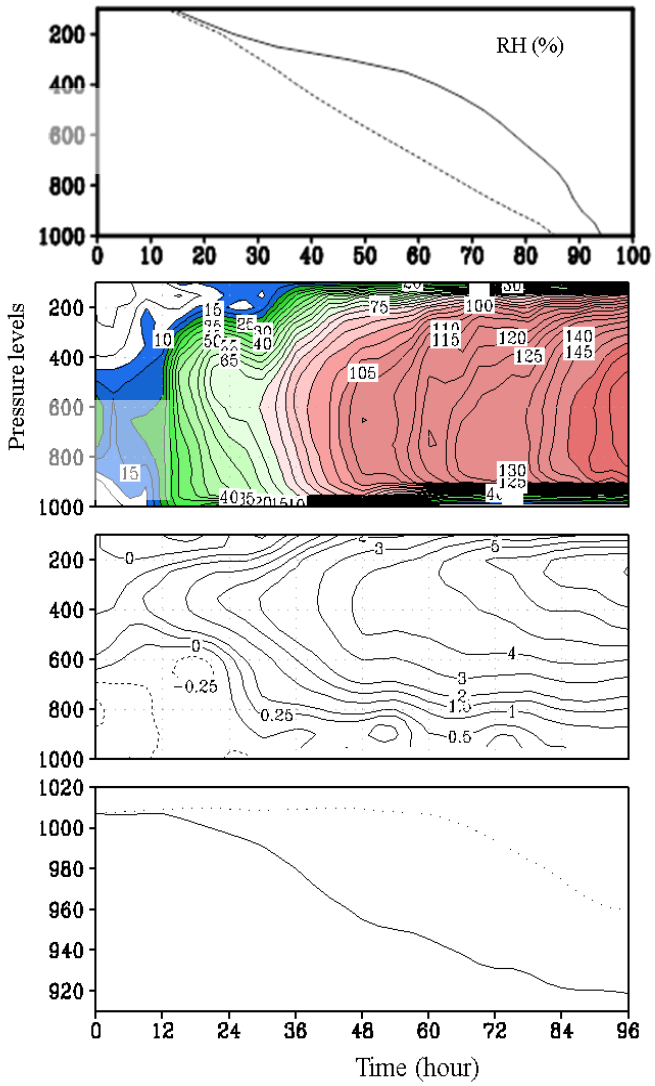

Fig. 6 (a) The environmental relative humidity (%) profile used in MID_VORTEX (dashed line) and MOIST (solid line). (b-d) Time-vertical pressure level (hPa) cross section of mean values of inner-core variables averaged over a 100km×100km box for (b) relative vorticity (1×10^{-5} s^{-1}), (c) temperature anomaly (°C), and (d) MSLP (hPa) (MID_VORTEX: dashed line, MOIST: solid line). Shading highlights large relative vorticity area, closely following vorticity contours.

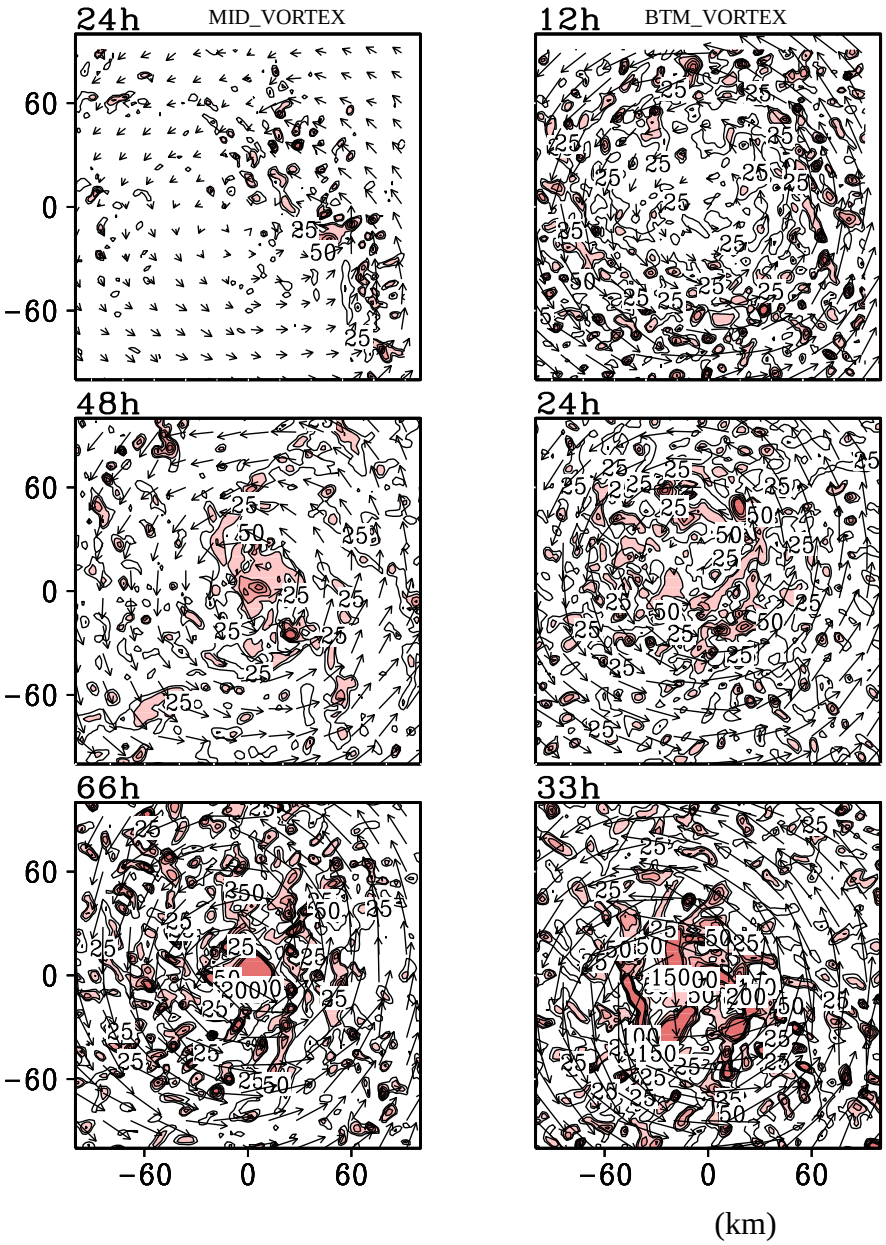

Fig. 7 The horizontal pattern of low-level (900hPa) wind field (vector) and relative vorticity (greater than $3\times10^{-4}s^{-1}$ are shaded) in MID_VORTEX (left) and BTM_VORTEX (right).

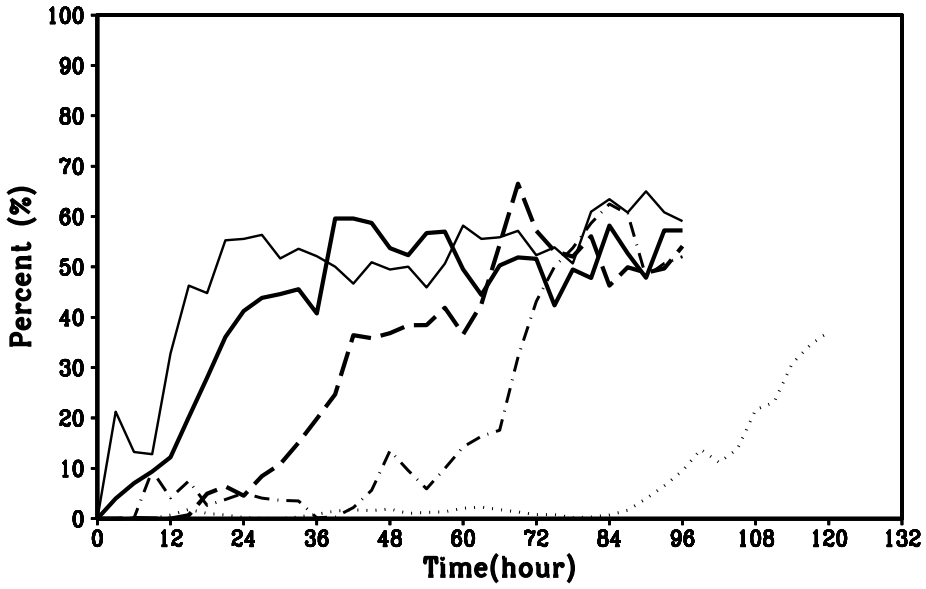

Fig. 8 The ratio of area of relative vorticity greater than $3\times10^{-4}\,s^{-1}$ within a 180km by 180 km domain in MOIST (thin solid line), BTM_VORTEX (thick solid line), MID_VORTEX (dashed line), SHAL_BTM (dot-dashed line) and SHAL_MID (dotted line).

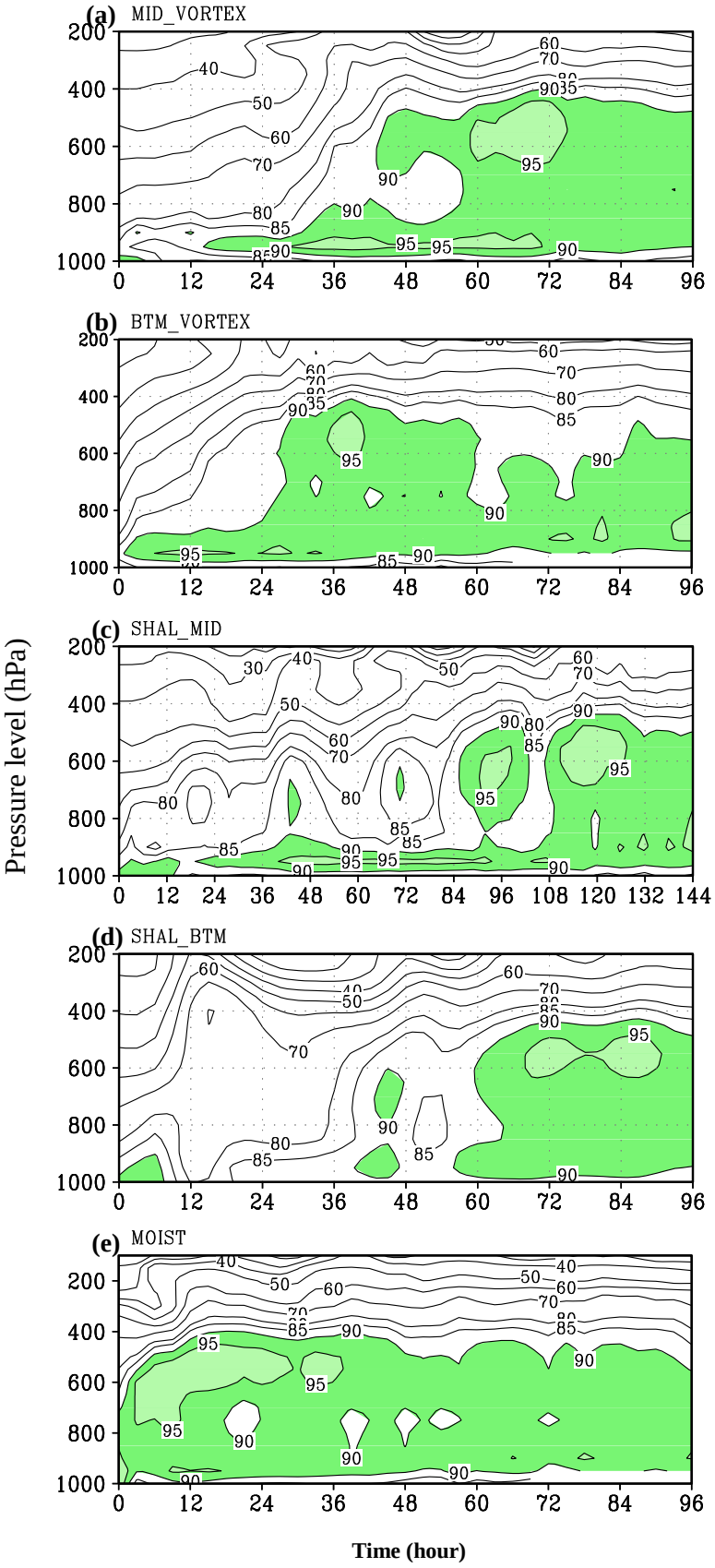

Fig. 9 Time-vertical pressure level (hPa) cross section of RH (%) averaged over a 100 km×100km box centered at the MSLP in each experiment. Shading highlights large relative humidity areas that exceed 90%.

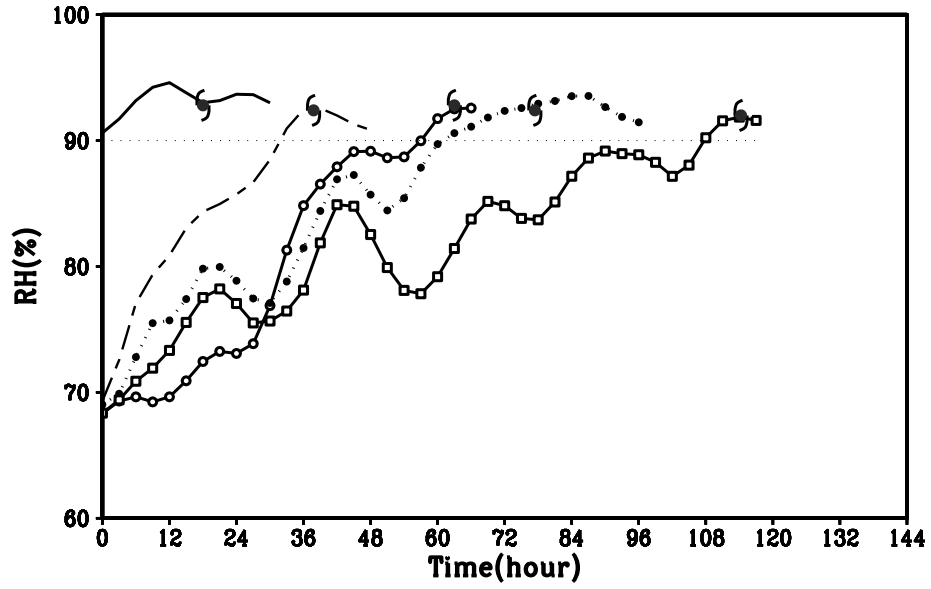

Fig. 10 Time evolution of the column averaged $\overline{RH}$ (from the surface to 500hPa, averaged over a 100 km×100km box centered at the MSLP) in MOIST (solid line), BTM_VORTEX (long dashed line), MID_VORTEX (solid line with open circle), SHAL_BTM (dotted line with solid circle), SHAL_MID (solid line with open square), respectively. The hurricane symbols represent the genesis timing for each experiment. .

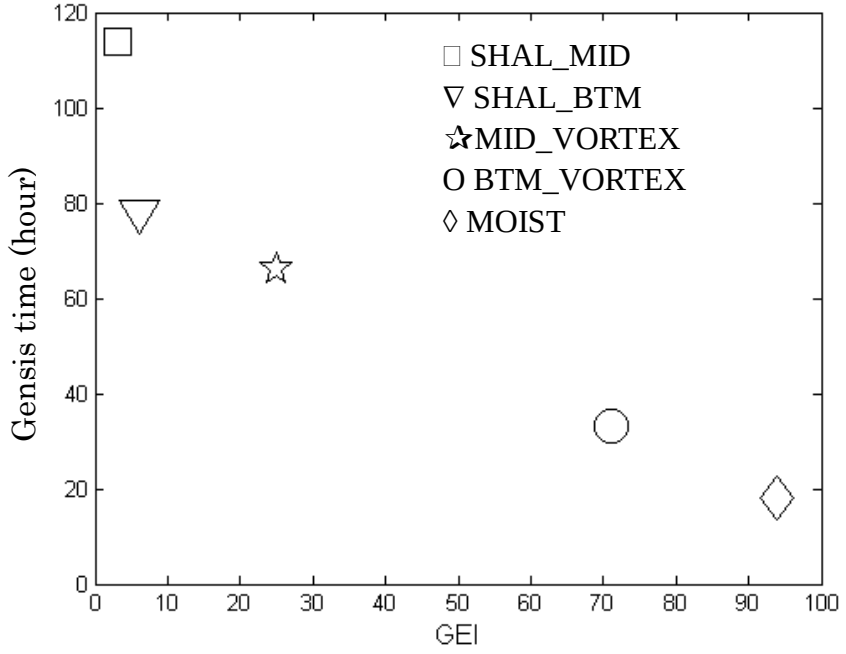

Fig. 11 The diagram shows the relationship of GEI to the genesis timing in the five experiments.

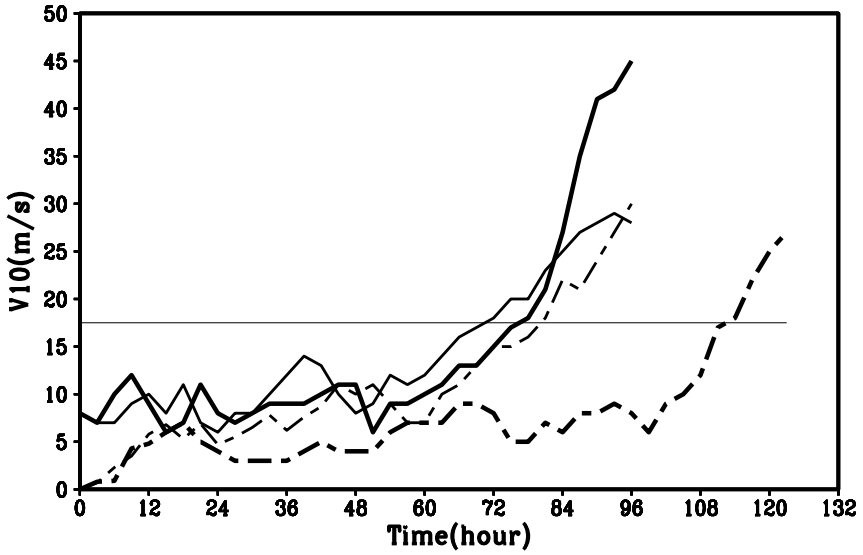

Fig. 12 Time evolution of maximum surface wind speeds in SHAL_BTM (thick solid line), SHAL_BTM8 (thin solid line), SHAL_MID (thick dashed line) and SHAL_MID8 (thin dashed line), respectively.

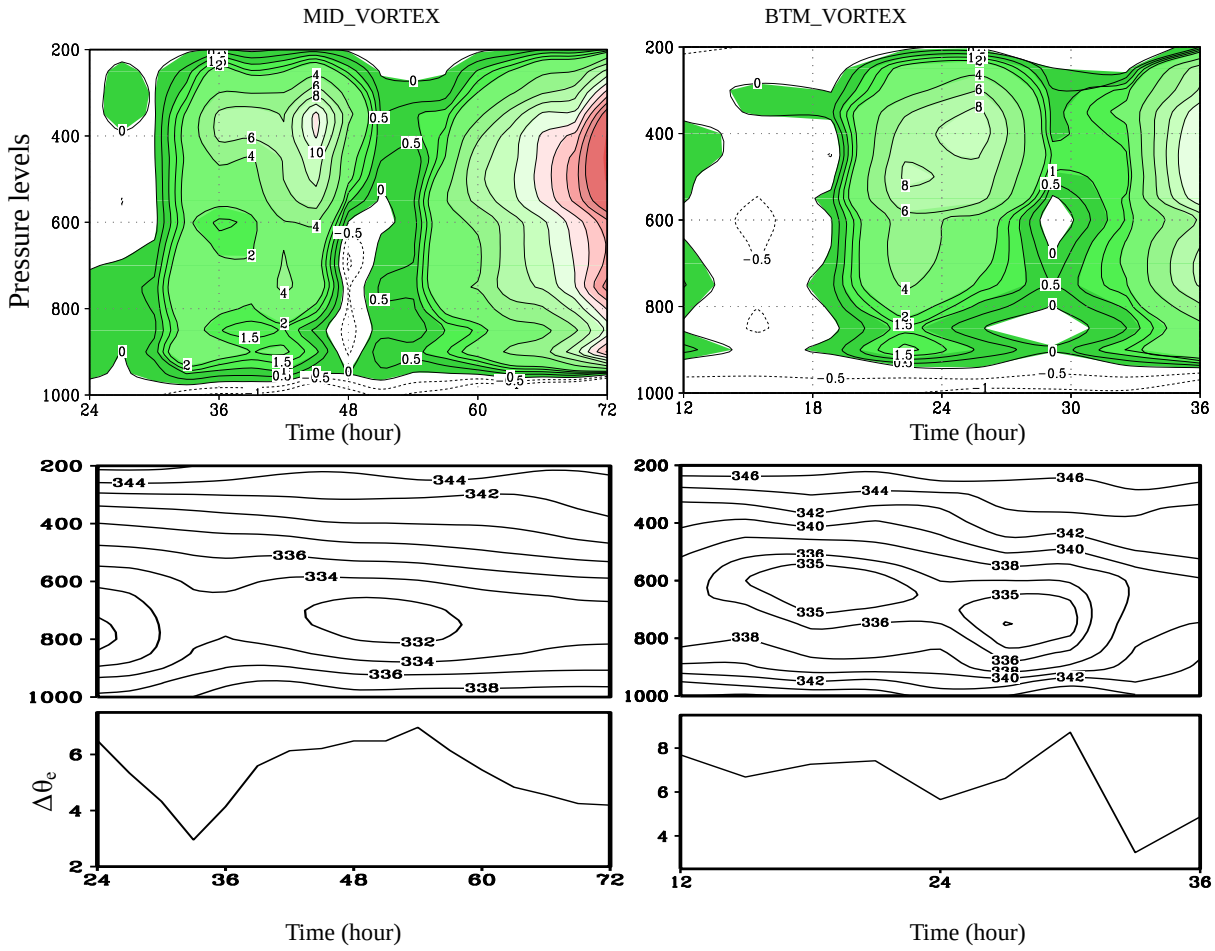

Fig. 13 Top: time-vertical cross section of latent heating rate (K/hr) averaged over a 100 km×100km box centered at the MSLP. Bottom: time-vertical cross section of θ_e (K) averaged over the same region and $\Delta\theta_e$ (defined as the difference of θ_e between 900 and 700hPa) in MID_VORTEX (left) and BTM_VORTEX (right). Different time periods are plotted in the horizontal axis for the two experiments.